iScience

Article

IFNγ signaling drives resistance to FLT3 inhibition in acute myeloid leukemia

Graphical abstract

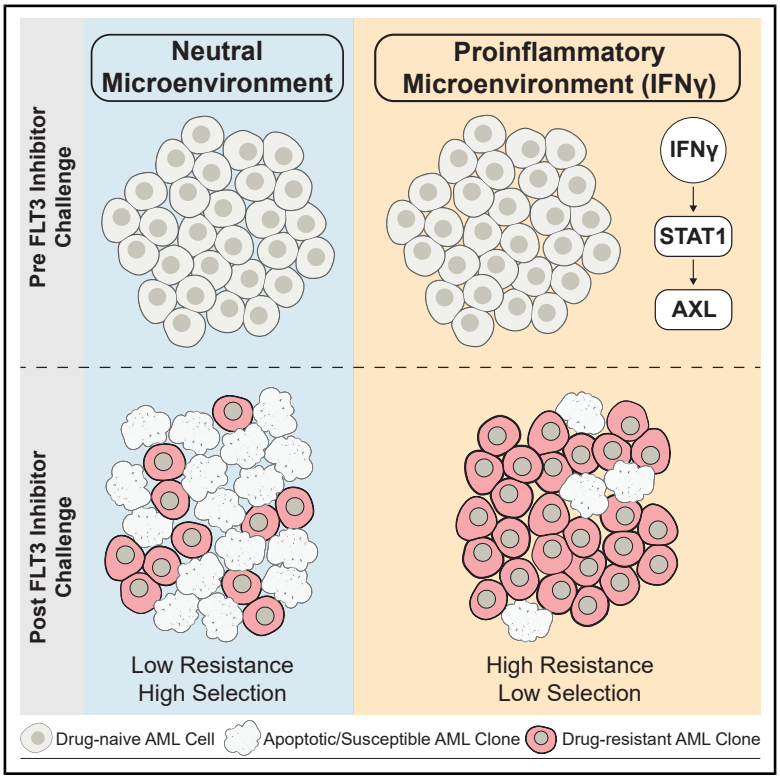

Highlights

- IFNγ signaling drives resistance to FLT3 inhibition in FLT3-ITD AML via STAT1 activation
- STAT1 activation upregulates AXL, providing an alternative survival pathway in AML
- Genomic barcoding reveals that IFNγ exposure expands drug-tolerant persister pools

Authors

Abraheem Khouqeer, Justin Cartailler, Christina Kim, ..., Anna E. Gilbert, Robert S. Welner, P. Brent Ferrell

Correspondence

brent.ferrell@vumc.org

In brief

Microenvironment; immunology; cell biology; cancer

Khouqeer et al., 2025, iScience *28*, 114079
December 19, 2025 Published by Elsevier Inc.
https://doi.org/10.1016/j.isci.2025.114079

CellPress

iScience

CellPress
OPEN ACCESS

Article

IFNγ signaling drives resistance to FLT3 inhibition in acute myeloid leukemia

Abraheem Khouqeer,[1,2,3] Justin Cartailler,[2] Christina Kim,[2] Kirsten M. Dickerson,[2] Chad R. Potts,[2,3] Anna E. Gilbert,[4] Robert S. Welner,[5] and P. Brent Ferrell[2,3,6,*]

[1]Program in Chemical and Physical Biology – Systems Biology, Vanderbilt University School of Medicine, Nashville, TN, USA
[2]Department of Medicine, Division of Hematology/Oncology & Vanderbilt-Ingram Cancer Center, Vanderbilt University Medical Center, Nashville, TN, USA
[3]Nashville Veterans Affairs Hospital, Tennessee Valley Health Care, Department of Veterans Affairs, Nashville, TN, USA
[4]Department of Biochemistry, Vanderbilt University School of Medicine, Nashville, TN, USA
[5]Division of Hematology/Oncology and O'Neal Comprehensive Cancer Center at the University of Alabama at Birmingham, Birmingham, AL, USA
[6]Lead contact
*Correspondence: brent.ferrell@vumc.org
https://doi.org/10.1016/j.isci.2025.114079

SUMMARY

Resistance to targeted therapies remains a major challenge in acute myeloid leukemia (AML). In *FLT3*-internal tandem duplication (*FLT3*-ITD) AML, FLT3 inhibitors such as quizartinib improve outcomes, but resistance limits long-term efficacy. While genetic resistance mechanisms are well characterized, the role of the bone marrow microenvironment remains unclear. We investigated how a pro-inflammatory microenvironment influences FLT3 inhibitor resistance and identified IFNγ as a key driver. IFNγ signaling activates STAT1, which in turn upregulates AXL, allowing leukemia cells to survive despite FLT3 inhibition. Knockdown, genomic degron tagging, and overexpression cell models confirmed STAT1 and AXL roles as mediators of resistance. Finally, analysis of IFNγ signaling and resistance in patient-derived AML blasts revealed variable sensitivity, suggesting the presence of additional compensatory mechanisms. These findings reveal IFNγ signaling as a mechanism of resistance, highlighting a potential therapeutic vulnerability in *FLT3*-mutated AML.

INTRODUCTION

Acute myeloid leukemia (AML) is a heterogeneous malignancy, with ~25% of cases harboring *FLT3*-internal tandem duplication (*FLT3*-ITD) mutations.[1–4] *FLT3* mutations confer poor prognosis due to enhanced proliferation and relapse.[5] While inhibitors like quizartinib and gilteritinib show efficacy, resistance limits survival.[6,7] Beyond genetic causes, such as secondary *FLT3* mutations and RAS/MAPK pathway alterations, increasing evidence highlights the role of non-genetic resistance mechanisms driven by the microenvironment.[6,8,9]

The bone marrow microenvironment shapes leukemia cell behavior and influences therapy response.[8] Pro-inflammatory microenvironments can promote AML progression and therapy resistance by providing pro-survival signals that enable leukemia cells to evade drug-induced apoptosis.[10–12] However, the role of pro-inflammatory signaling in FLT3 inhibitor resistance, particularly in response to quizartinib, remains poorly understood.

Non-genetic resistance mechanisms allow AML cells to persist despite FLT3 inhibition, often through adaptive cellular states that precede permanent resistance. One such adaptive state involves drug-tolerant persister (DTP), which can withstand drug exposure and serve as a reservoir from which fully resistant clones emerge.[13–15] Cytokine-mediated signaling, such as STAT5 activation, has been implicated in promoting non-genetic resistance to quizartinib, enabling AML cells to bypass FLT3 inhibition through alternative survival pathways.[16]

Using IC_{50} assays, genomic barcoding, genomic degron tagging, and longitudinal drug challenge assays, we identified IFNγ as a key driver of resistance, acting through STAT1-dependent upregulation of AXL, a receptor tyrosine kinase (RTK).[16–19]

To assess clinical relevance, we investigated *FLT3*-mutated AML blasts from 20 patients under inflammatory conditions. These experiments revealed significant heterogeneity, suggesting that while AXL plays a prominent role, additional compensatory pathways may contribute to resistance in a patient-specific manner. Our findings highlight pro-inflammatory signaling's role in FLT3 inhibitor resistance, offering insights for combination or precision therapies.

RESULTS

IFNγ induces resistance in AML cell lines exposed to *FLT3*-ITD AML-targeting therapeutics

To investigate the implications of non-genetic resistance in *FLT3*-ITD AML driven by the microenvironment, an IC_{50} assay was developed to map the response landscape across clinically approved chemotherapeutic drugs and *FLT3*-ITD

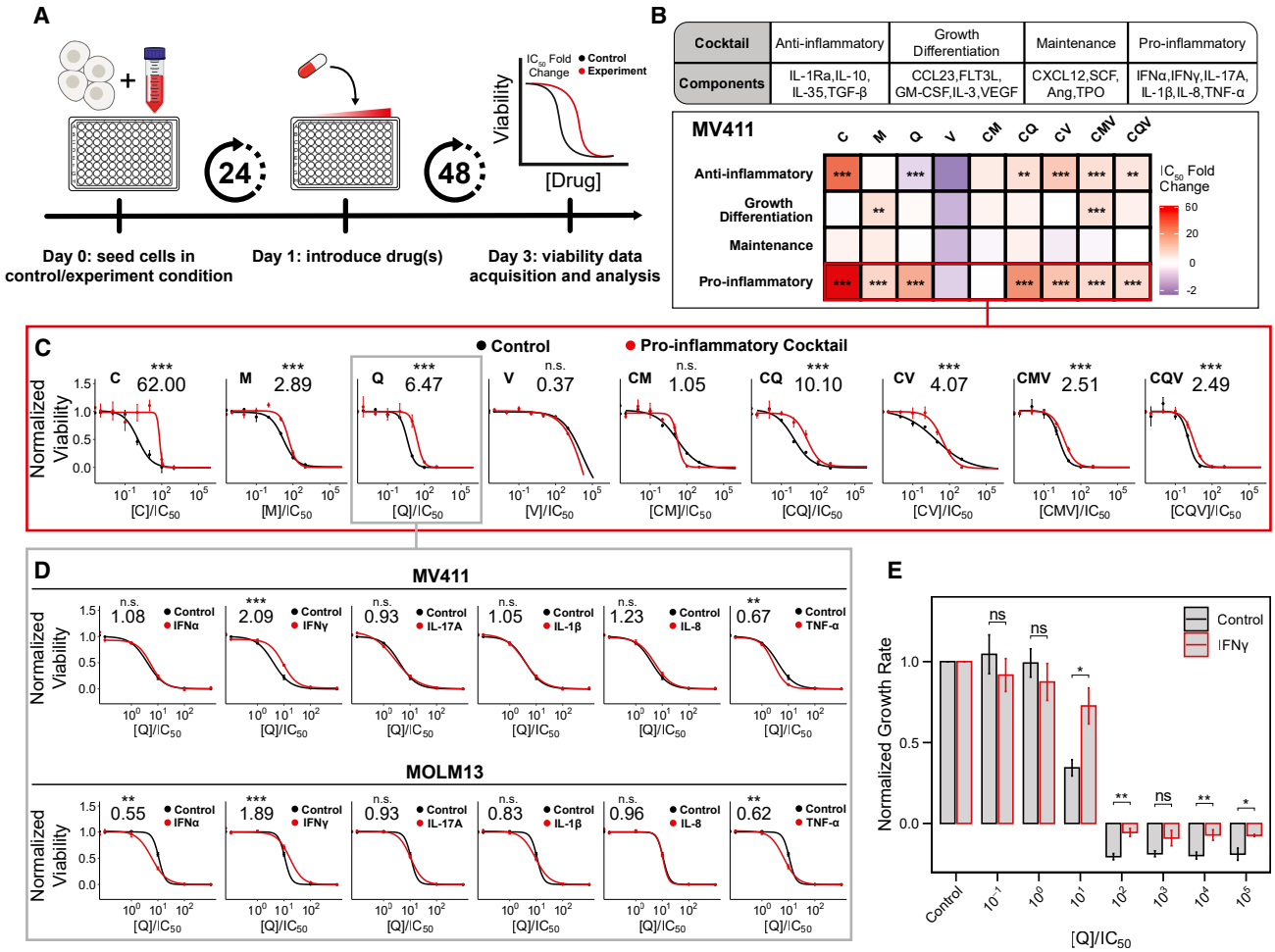

Figure 1. Impact of microenvironment on drug dose-response viability in *FLT3*-ITD AML cell lines

(A) Experimental workflow: cells were seeded in the PBS control or experimental condition for 24 h, followed by drug exposure at log-scale incremental concentrations. Viability was assessed after 48 h of drug exposure using CellTiter-Glo 2.0.

(B) Experimental conditions for the IC_{50} assay, presented as cocktails of components representing distinct cellular microenvironments: anti-inflammatory, growth and differentiation, maintenance, and pro-inflammatory (top). The heatmap displays the IC_{50}-fold change between the control and respective cocktails in MV411 cells against drug or drug combinations (bottom). Drugs used are: (cytarabine: C), (midostaurin: M), (quizartinib: Q), and (venetoclax: V).

(C) IC_{50} fits for the pro-inflammatory cocktail, with fold changes displayed for each fit plot.

(D) IC_{50} fits for individual components of the pro-inflammatory cocktail in both MV411 and MOLM13 cell lines.

(E) Normalized growth rates of MV411 cells measured between 24 and 72 h post-drug exposure at the specified dosages under control and IFNγ conditions. Statistical significance for the IC_{50} ratios and normalized growth rates was determined using an independent samples *t* test, where $p < 0.05$ (*), $p < 0.01$ (**), $p < 0.001$ (***), and n.s. = not significant. Error bars represent the mean ± standard deviation from triplicate experiments.

AML-targeting small molecules under four primary microenvironmental cocktails: anti-inflammatory, growth and differentiation, maintenance, and pro-inflammatory (Figures 1A and 1B). The degree of microenvironmental influence on drug response is quantified as the fold change in IC_{50}. Figure 1B highlights the response landscape for the MV411 *FLT3*-ITD AML cell line (Figure S1A). The pro-inflammatory microenvironment consistently induced resistance across most drugs tested (Figure 1C), underscoring the critical role of pro-inflammatory signaling in *FLT3*-ITD AML. To pinpoint which component of the pro-inflammatory cocktail drive the resistance, we performed IC_{50} assays with individual components of the cocktail, focusing on quizartinib due to its clinical relevance and potency as a FLT3 inhibitor. Assays were conducted on two *FLT3*-ITD AML cell lines, MV411 and MOLM13 (Figure 1D). IFNγ emerged as the dominant driver of resistance. To investigate potential synergistic effects of IFNγ with other components, we conducted additional assays combining IFNγ with exactly one other pro-inflammatory cocktail component (Figure S1B). Results confirmed that IFNγ is essential for the resistance response, with minimal contribution from other components. To evaluate the impact of different microenvironments on proliferation, we also quantified the relative proliferation capacity (Figures S1D and S1E). Lastly, we assessed the growth rate of MV411 cells across drug concentrations under control and IFNγ conditions (Figure 1E). Cells exposed to IFNγ exhibited significantly higher

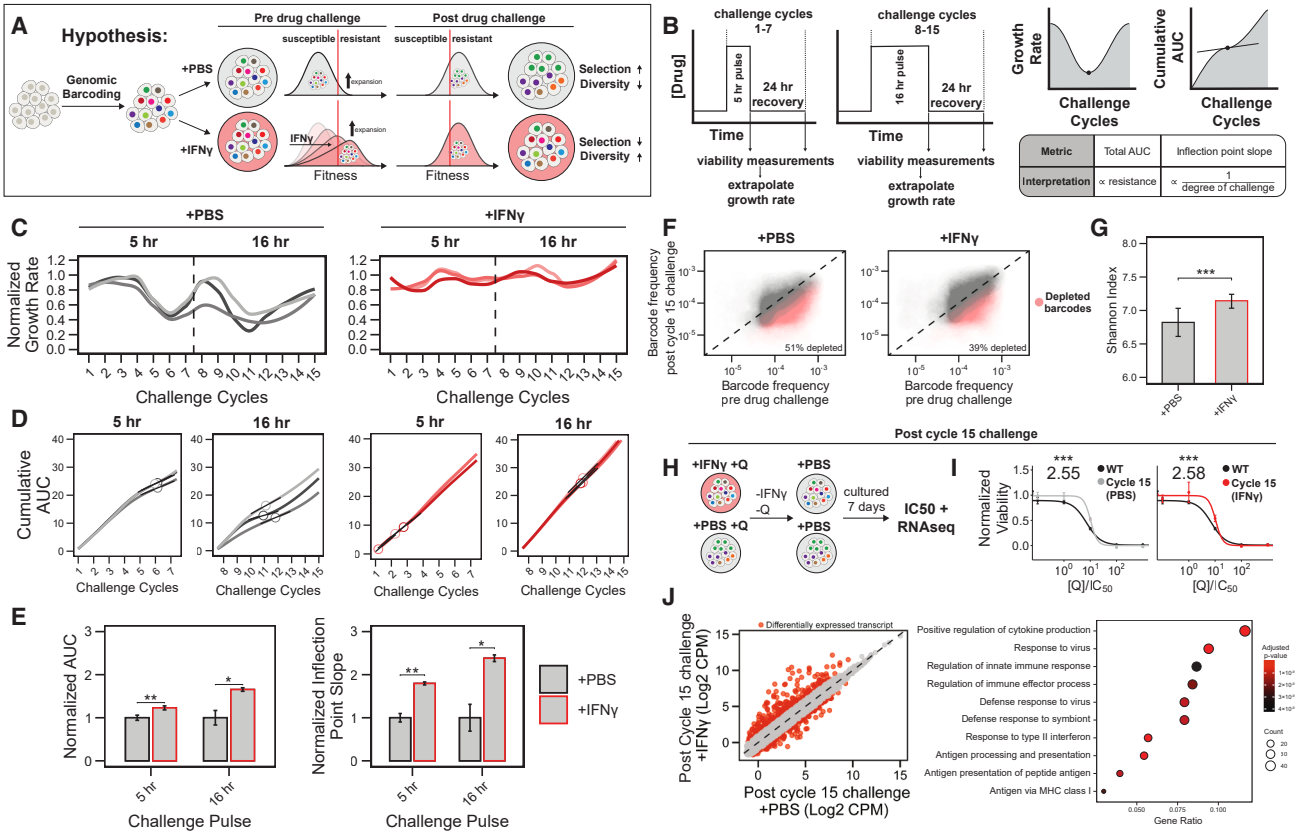

Figure 2. IFNγ shifts cells to a drug resistance state and maintains population diversity in MV411 cells during sequential quizartinib drug challenge cycles

(A) Hypothesis and experimental approach: using genomic barcoding, we tested whether IFNγ shifts cells to a drug-resistant state during challenge cycles, leading to less selection and greater diversity compared to the PBS control.

(B) Drug challenge assay workflow: the assay consists of 15 challenge cycles split into two phases, 5-h drug pulses for cycles 1–7 and 16-h pulses for cycles 8–15. Growth rate extrapolations over the challenge cycles were used to calculate the area under the curve (AUC), which is directly proportional to resistance. The cumulative AUC highlights the inflection point in the challenge cycles, with the slope at the inflection point inversely proportional to the degree of challenge (see materials and methods).

(C) Normalized growth rate of MV411 cells across quizartinib (Q) challenge cycles for PBS and IFNγ conditions with data smoothed using a locally weighted smoothing function. Each curve represents a replicate experiment.

(D and E) Cumulative AUC for the two sequential phases of quizartinib challenge cycles, with the slope at the inflection point quantified. Error bars represent the mean ± standard deviation from triplicate experiments.

(F) Barcode frequency in log scale for MV411 cells pre- and post-15 cycles of quizartinib challenge under PBS control and IFNγ conditions.

(G) Shannon Index of barcode diversity in the two conditions, with error bars represent the bootstrap estimate of standard error.

(H) Post-challenge workflow: after 15 drug challenge cycles, cells were maintained in control media for seven days, followed by IC_{50} assays (I) and RNA sequencing with gene ontology (GO) analysis (J). Statistical significance for IC_{50} ratios and challenge metrics was assessed using independent samples *t* test, where $p < 0.05$ (*), $p < 0.01$ (**), $p < 0.001$ (***), and n.s. = not significant.

growth rates at effective drug doses compared to control, further validating the critical role of IFNγ in mediating resistance.

Microenvironmental IFNγ reprograms AML populations toward a resistant state

To assess whether the IFNγ-induced shift in IC_{50} contributes to microenvironment-driven resistance, we employed a genomic barcoding strategy to track clonal selection in conjunction with a drug-pulse challenge cycles assay designed to mimic *in vivo* drug bioavailability, a model previously shown to promote the emergence of resistant clones.[20–23] We hypothesized that the IC_{50} shift under IFNγ would indicate that a greater proportion of the IFNγ-exposed population would withstand drug challenge relative to the PBS-treated population. To test this, we exposed genomically barcoded cells to repeated drug treatment cycles, beginning with 5-h pulses until growth rates returned to baseline (∼2.5 weeks), followed by 16-h pulses until baseline was restored again (∼3.4 weeks) (Figures 2A and 2B). The normalized growth rate during recovery was used to assess susceptibility versus resistance through two metrics: the area under the curve (AUC) of the growth rate over time, where a larger AUC indicated greater resistance, and the slope at the inflection point, representing the challenge experienced by the cell population. A steeper slope reflected faster recovery and lower challenge,

while a shallower slope indicated greater challenge and prolonged adaptation. Under PBS control conditions, the population displayed a clear decline in growth rate with increasing cumulative challenge cycles (Figure 2C). This effect was abolished under IFNγ conditions. In both 5- and 16-h challenge cycles, the AUC was higher for cells exposed to IFNγ, indicating greater resistance. Additionally, the slope at the inflection point was steeper under IFNγ conditions, suggesting that cells in this condition experienced less challenge compared to the PBS control (Figures 2D and 2E). After 15 challenge cycles, clonal population diversity was assessed by sequencing genomic barcodes and comparing them to the pre-challenge population. Accounting for a 25% random barcode dropout based on previous reports, barcode depletion was higher under PBS control conditions (51%) compared to IFNγ conditions (39%) (Figure 2F).[24,25] This finding was corroborated by the Shannon diversity index, which demonstrated greater diversity in the IFNγ condition (Figure 2G). To determine whether the acquired resistance in IFNγ-treated cells depended on IFNγ, cells were maintained in drug-free control media for 7 days to eliminate exogenous signals. Notably, we found that the resistance levels (IC_{50}) between the two conditions were comparable after this seven-day washout, suggesting that the acquired resistance was independent of sustained IFNγ exposure. This suggests that IFNγ enabled more cells within the population to acquire resistance—a novel observation not previously reported (Figures 2H and 2I). Finally, transcriptional profiling revealed distinct differences between the two conditions. Cells exposed to IFNγ displayed a transcriptional profile resembling a 24-h IFNγ exposure (Figures 2J and S2A–S2F). This suggests residual IFNγ-related signaling, potentially mediated by chromatin remodeling or other adaptive mechanisms.[26] These data suggest that while both PBS and IFNγ conditions ultimately achieve comparable resistance levels, IFNγ decreased the quizartinib selection pressure and shifted the population fitness toward a more drug resistant state.

STAT1 signaling drives IFNγ-induced resistance, with AXL as the key mediator

Having established that IFNγ induces resistance to quizartinib, we sought to investigate the underlying mechanism. Prior studies have demonstrated that STAT1, a transcription factor downstream of IFNy signaling, can contribute to the acquired resistance potentially by upregulation of other RTKs (Figure 3A).[27] To establish a causal link between IFNγ-STAT1 signaling and resistance, we engineered MV411 cell line with degron-tagged STAT1 (Figure 3B). This enabled us to abolish STAT1 activity within hours, thus minimizing compensatory signaling seen with other methods, and directly assess its role in IFNγ-induced resistance.[28,29] The degron function was verified via western blot analysis using the degron degrader dTAG-13 (d13) (Figure 3C). Using this modified cell line, we conducted IC_{50} assays under degraded STAT1 conditions and observed that IFNγ-induced resistance was abolished (Figure 3D). Additionally, the growth rate across drug doses in STAT1-degraded cells aligned with that of the PBS control, confirming that STAT1 is a dominant driver of IFNγ-induced resistance (Figure 3E).

Previous studies have suggested that AXL, an RTK upregulated in response to IFNγ, may function redundantly to enable cells to bypass FLT3 inhibition.[16,30–32] To investigate AXL's role in resistance, we examined its two primary modes of activation: ligand-dependent and ligand-independent mechanisms (Figure 3F).[17] As a first step, we confirmed that IFNγ exposure led to AXL upregulation in MV411 and MOLM13 cells (Figure 3G). Additionally, we assessed AXL expression following treatment with the JAK1/2 inhibitor ruxolitinib and found that AXL expression was downregulated in its presence, further supporting a connection between JAK/STAT1 signaling and AXL regulation (Figure S3A).[33] We then performed IC_{50} assays in the presence of bemcentinib, an AXL inhibitor, which abolished resistance under IFNγ conditions (Figure 3H).[34] Similarly, shRNA-mediated AXL knockdown eliminated IFNγ-induced resistance, supporting AXL's critical role. To test the ligand-dependent mechanism, we introduced AXL-Fc/soluble AXL (sAXL), which binds the AXL ligand GAS6, rendering it unable to bind endogenous AXL.[16] Despite the addition of sAXL, IFNγ-induced resistance persisted. GAS6 knockdown via shRNA produced similar results, and a GAS6 ELISA performed on supernatants from control and IFNγ-exposed cells detected no GAS6 in either condition (data not shown). We then investigated the ligand-independent mechanism of AXL activation. Overexpression of RTKs, including AXL, is known to trigger autophosphorylation and activation.[35,36] Indeed, AXL overexpression in our system resulted in a more pronounced shift in IC_{50} compared to the wild-type (WT) cell line. These findings suggest that STAT1 signaling plays a critical role in IFNγ-induced resistance, with AXL likely acting through a ligand-independent mechanism and serving as a key contributor.

Gilteritinib abolishes IFNγ-induced resistance, but introduces IFNγ-dependent selection of highly proliferative resistant clones

Having established AXL as a major contributor to IFNγ-induced resistance, we hypothesized that gilteritinib, a dual FLT3 and AXL inhibitor, would abolish the induced resistance and produce a selection profile in the drug-pulse challenge assay resembling the PBS control (Figure 4A). To test this, we expanded upon the screen in Figure 1 by performing IC_{50} assays using gilteritinib and its combinations (Figure 4B). Consistent with prior observations, the pro-inflammatory cytokine cocktail induced gilteritinib resistance in MV411 cells (Figure S4A). However, when individual components were tested, including IFNγ, no significant shifts in IC_{50}-fold change were observed in either MV411 or MOLM13 cells (Figure 4C). These findings suggest that resistance may be driven by parallel inflammatory pathways with potential crosstalk, acting independently of RTKs, as previously observed with quizartinib.

We further examined the hypothesis using a drug challenge assay similar to the one used for quizartinib (Figure 2). While the PBS control condition displayed the expected decrease in growth rate with increasing challenge cycles, IFNγ-exposed cells did not align with the control as hypothesized (Figure 4D). Instead, there appeared to be a selection for highly proliferative cells during the 5-h pulse cycles. These selected cells demonstrated increased resistance, indicated by a higher AUC and a lower degree of challenge, as reflected by the slope at the inflection point (Figures 4E–4G).

Genomic barcoding revealed interesting insights. Although the decrease in population growth rate suggests that gilteritinib

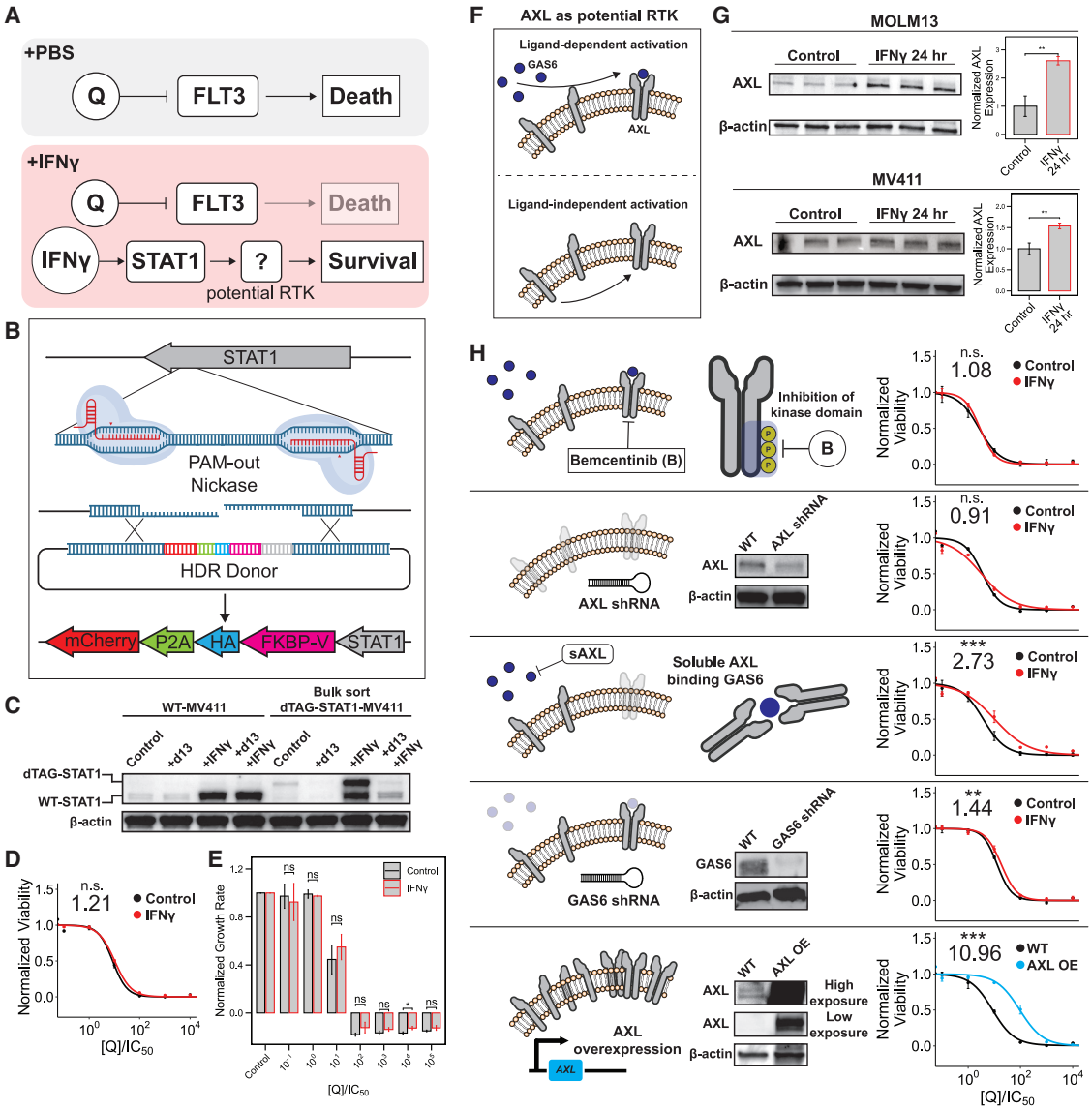

Figure 3. STAT1 signaling drives IFNγ-induced resistance via AXL expression and ligand-independent activation

(A) Schematic of the model linking IFNγ-induced STAT1 signaling to resistance via receptor tyrosine kinase (RTK) activation.

(B) CRISPR-Cas9 PAM-out Nickase strategy to introduce a homology-directed repair (HDR) cassette encoding an FKBP degron tag at the N-terminus of STAT1.

(C) Validation of STAT1 degradation using dTAG degrader (d13, 100 ng/mL) in WT and bulk sorted engineered MV411 (dTAG-STAT1-MV411) cells exposed to d13, IFNγ (10 ng/mL), or both for 24 h. WT-STAT1 and dTAG-STAT1 abundance were analyzed via Western blotting.

(D) IC_{50} assay of homozygous dTAG-STAT1 edited MV411 treated with d13 (100 ng/mL) for 24 h under control or IFNγ conditions.

(E) Normalized growth rates of homozygous dTAG-STAT1 MV411 treated with d13 measured between 24 and 72 h post-drug exposure at specified dosages in control and IFNγ conditions.

(F) Schematic of AXL as a candidate RTK and its activation mechanisms: ligand-dependent and ligand-independent.

(G) Western blot and quantification of AXL expression in MOLM13 and MV411 cells after 24-h exposure to IFNγ, with experiments performed in triplicates.

(H) IC_{50} assay results for MV411 cells modified with the following conditions (top to bottom): bemcentinib (61.8 nM) to inhibit AXL kinase activity, AXL knockdown via shRNA, addition of soluble AXL (sAXL, 2 μg/mL) to neutralize GAS6 ligand, GAS6 knockdown via shRNA, and AXL overexpression. Statistical significance for the IC_{50} ratios and normalized growth rates was determined using an independent samples *t* test, where $p < 0.05$ (*), $p < 0.01$ (**), $p < 0.001$ (***), and n.s. = not significant. Error bars in all panels represent the mean ± standard deviation from triplicate experiments. IC_{50} values are summarized in Data S1.

broadly eliminated cells, the minimal barcode depletion indicates a lack of preferential clonal selection. In contrast, the IFNγ condition exhibited substantial barcode depletion and a lower Shannon Index (Figures 4H and 4I), indicating a higher degree of selection. This was further supported by the growth rate observed in the challenge assay, which reflected the selection of highly proliferative clones. To evaluate whether the magnitude of resistance differed post-challenge, both PBS control and

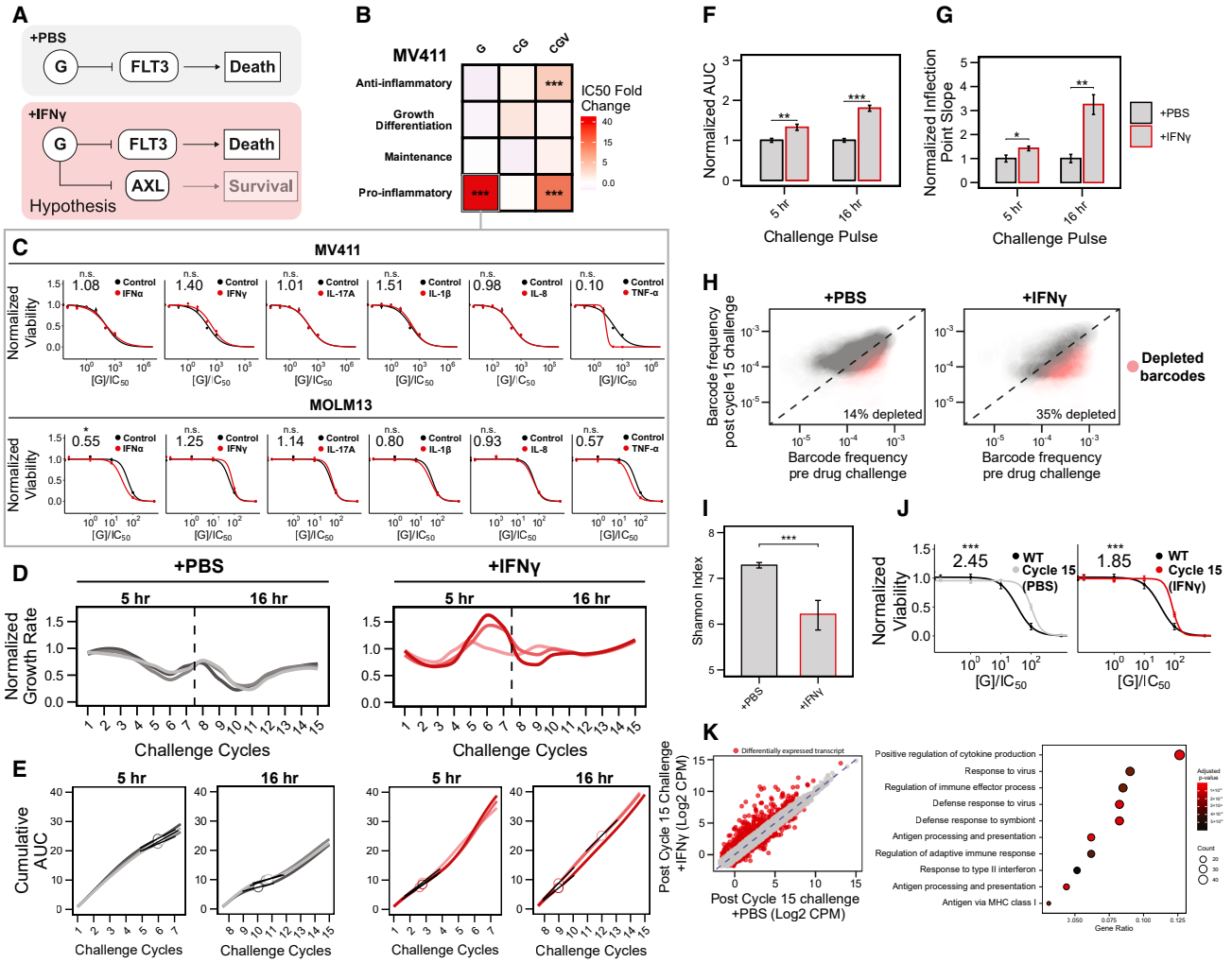

Figure 4. Gilteritinib reduces IFNγ-induced resistance in *FLT3*-ITD AML cells, but selects for highly proliferative clones

(A) Schematic of the signaling model hypothesizing that gilteritinib through dual inhibition of FLT3 and AXL, abolishes IFNγ-induced resistance.

(B) Heatmap showing IC_{50}-fold change of gilteritinib and its combinations across different microenvironmental cocktails in MV411 cells.

(C) Gilteritinib (G) IC_{50} fits for individual components of the pro-inflammatory cocktail in both MV411 and MOLM13 cell lines.

(D) Normalized growth rates of MV411 cells across gilteritinib challenge cycles under PBS and IFNγ conditions, with data smoothed using a locally weighted smoothing function. Each curve represents a replicate experiment.

(E–G) Cumulative AUC for the two sequential phases of gilteritinib challenge cycles, with slopes at the inflection point quantified. Error bars represent the mean ± standard deviation from triplicate experiments.

(H) Barcode frequency in log scale for MV411 cells before and after 15 cycles of gilteritinib challenge under PBS control and IFNγ conditions.

(I) Shannon index of barcode diversity between the conditions, with error bars representing the bootstrap estimate of standard error. After 15 challenge cycles, cells were maintained in control media for seven days before IC_{50} assays (J) and RNA sequencing with GO term analysis (K). Statistical significance for IC_{50} ratios and challenge metrics was assessed using independent sample *t* test, where $p < 0.05$ (*), $p < 0.01$ (**), $p < 0.001$ (***), and n.s. = not significant. Error bars in IC_{50} experiments indicate the mean ± standard deviation from three independent replicates.

IFNγ-exposed populations were maintained in control media for seven days following the 15 challenge cycles. Interestingly, the resistance magnitude between the two conditions differed, with IFNγ-exposed cells exhibiting a lower fold-change relative to WT (Figure 4J). This suggests that while the IFNγ condition displayed higher resistance during the assay, this resistance was dependent on continuous IFNγ exposure. Transcriptional profiling showed results like those observed in the quizartinib assay (Figure 2), suggesting that transcriptional changes may play a more critical role in resistance under gilteritinib treatment compared to quizartinib (Figures 4K and S4B–S4G).

Translational relevance of IFNγ-induced resistance in *FLT3*-mutated AML patient blasts

To connect the mechanistic insights observed in cell lines to AML, we designed an experimental and analysis workflow to examine *FLT3*-mutated AML patient blasts. Bone marrow samples with high blast counts were cultured for 5–7 days in blast

media to establish a uniform baseline, enabling more robust and controlled experiments (Figure 5A). We assessed multiple dimensions to characterize the patient blasts. We defined AML cell ontogeny using six key surface markers from a ten-marker panel in spectral flow cytometry, comparing them to healthy bone marrow to precisely determine their position along the differentiation spectrum (Figure S7). The phosphorylation of STAT1 (pSTAT1) in response to IFNγ was measured to evaluate activation of the IFNγ-STAT1 signaling cascade. pSTAT1 responses were also quantified using flow cytometry and analyzed with SARAR (Figure S8).[37] We also investigated the IC_{50} shifts for both quizartinib and gilteritinib with and without IFNγ, as well as AXL expression in response to IFNγ (Figures S9–S11A). Figures 5B–5E display representative data of the analyses. The analysis was integrated into a summary map for each patient blast sample (B#), with quantitative measures presented as percentages, fold changes, or *Z* scores (Figure 5F).

We observed a positive correlation between pSTAT1 levels and AXL expression, highlighting the importance of IFNγ signaling in driving AXL expression (Figure 5G), particularly in monocyte-classified blasts (Figure S11B). This positive correlation was also associated with the proliferative capacity of the samples and their baseline gilteritinib IC_{50} (Figure S11C). Stratifying blasts by baseline gilteritinib IC_{50} using z-scores revealed that samples in the high IC_{50} group exhibited significantly lower AXL fold change in response to IFNγ compared to the low IC_{50} group (Figure 5H). This suggests that samples with higher resistance to gilteritinib may not rely on downstream IFNγ signaling for survival. In contrast, blasts with low baseline quizartinib IC_{50} displayed a fold-change shift upon IFNγ exposure (Figure 5I). Conversely, the fold-change shift in gilteritinib IC_{50} was inversely proportional to the baseline gilteritinib IC_{50} (Figure S11D). These findings underscore the heterogeneity of AML, even under tightly controlled experimental conditions. Nonetheless, the observed correlations emphasize key cellular mechanisms underlying resistance in specific patient samples, providing critical insight into potential therapeutic strategies.

DISCUSSION

The microenvironment plays a critical role in driving resistance to targeted therapies, yet its contribution to *FLT3*-ITD AML remains largely uncharacterized.[6,8,9] While studies on short-term microenvironmental influences provide valuable insights into the cell's response to drug, they fail to capture the long-term dynamics of resistance.[8] Understanding how resistance evolves over time is essential, as it reflects the selective pressures and adaptive changes that occur in physiological systems, including clinical settings.

Here, we demonstrate that IFNγ, a key inflammatory cytokine, induces resistance in short term FLT3 inhibitors in IC_{50} assays. However, beyond this acute response, we uncover novel insights into how resistance manifests over extended periods. Genomic barcoding and longitudinal drug challenge assays revealed that IFNγ exposure increases the fraction of AML cells entering a quizartinib-resistant state, as shown by barcode diversity analysis. In contrast, under control conditions, the majority of cells remain sensitive to quizartinib, with only a subset displaying resistance. DTP cells, a subpopulation of cancer cells capable of surviving drug exposure, provide a reservoir from which resistant clones can emerge through genetic or non-genetic mechanisms.[14,25,30] Our findings suggest that IFNγ increases the pool of DTP cells, thereby heightening the likelihood of resistance development via either genetic evolution or adaptive mechanisms.[38,39]

Transcriptional analysis of what may be classified as DTP cells post-drug challenge revealed persistent resistance even after IFNγ removal, indicating an adaptive rather than transient effect, potentially driven by epigenetic reprogramming or an autocrine process.[26,40] While the limited efficacy of AML therapies *in vivo* is often attributed to limited drug accessibility within bone marrow niches, our findings suggest that microenvironmental signaling reprograms leukemia cell responses to treatment, altering drug sensitivity and promoting persistence.[41,42]

Mechanistically, we identify the IFNγ-STAT1 axis as the primary driver of IFNγ-induced resistance. While previous studies have implicated AXL in FLT3 inhibitor resistance via its ligand GAS6 and cytokine-dependent STAT5 activation, our findings reveal a distinct, ligand-independent pathway.[16] Specifically, IFNγ-mediated STAT1 activation drives AXL upregulation, providing an alternative survival pathway. This is supported by both genetic and pharmacological interventions, which demonstrate that both STAT1 degradation and AXL inhibition abolish IFNγ-induced resistance. These findings highlight how AML cells exploit inflammatory signaling pathways to activate alternative survival mechanisms, positioning AXL as a key mediator of resistance in this context. Furthermore, AXL overexpression resulted in an even greater resistance shift, suggesting that AXL-driven resistance functions along a continuum rather than as a binary, switch-like mechanism. This observation is consistent with the ligand-independent dimerization model of RTK activation, where receptor overexpression increases random encounters, leading to activation and downstream signaling.[35,43,44] The presence of multiple mechanisms driving AXL upregulation and resistance underscores the multimodal complexity by which the microenvironment contributes to therapy resistance. While AXL appears to be a primary driver in this system, we speculate that other RTKs or combinations of RTKs could similarly contribute to resistance through cross-activation when overexpressed. Furthermore, the possibility that FLT3 inhibitors exhibit off-target effects on additional RTKs may further complicate the resistance landscape and should be considered when interpreting inhibitor responses.[28,29]

Our findings also reveal an unexpected limitation of gilteritinib as a dual FLT3/AXL inhibitor.[42] While gilteritinib initially prevents IFNγ-induced resistance, prolonged drug exposure leads to the selection of highly proliferative resistant clones that exhibit a degree of dependence on IFNγ to maintain resistance. This suggests that although AXL inhibition effectively counteracts acute IFNγ-driven resistance, additional mechanisms, beyond RTKs, contribute to long-term adaptation.[8] Notably, this observation was only detectable through our genomic barcoding and longitudinal drug challenge assay, highlighting the importance of long-term tracking in uncovering adaptive resistance dynamics.

Expanding these observations to a translational context, we cultured AML patient blast samples and characterized both their

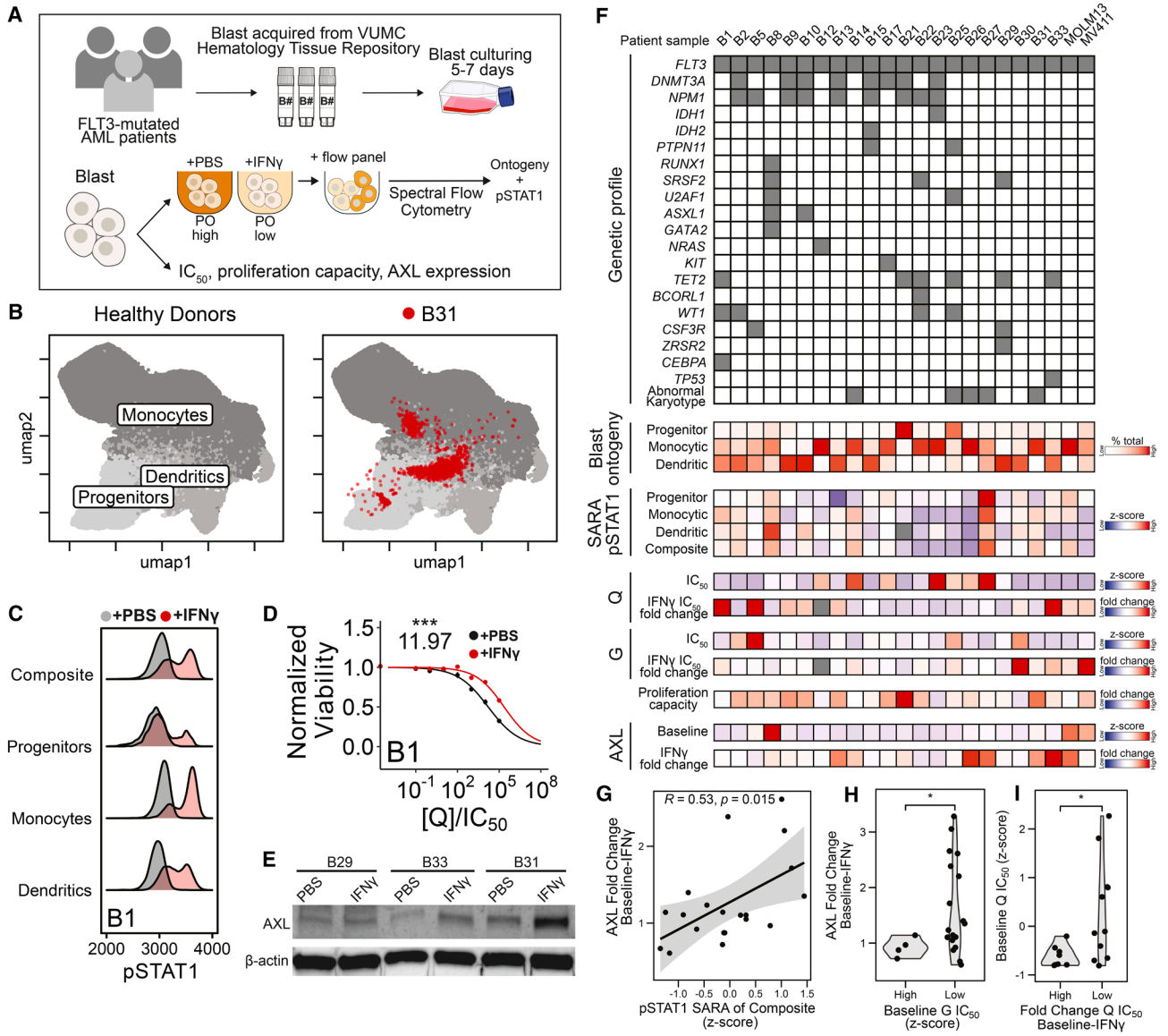

Figure 5. Translational relevance of IFNγ-induced resistance in *FLT3*-mutated AML patient blasts

(A) Workflow of experimental design: patient blasts obtained from the VUMC Hematology Tissue Repository were cultured for 5–7 days in blast media. A subset of cells was stimulated with IFNγ and barcoded to be combined with control conditions, then analyzed via spectral flow cytometry to assess ontogeny and pSTAT1 response. Additional cells were used for IC_{50} assays with quizartinib and gilteritinib, proliferation capacity assessments, and AXL expression analysis (see materials and methods).

(B) Healthy donor bone marrow embedding of progenitors, dendritic cells, and monocytes (left). Representative patient blast projection onto the donor embedding to determine blast ontogeny (right).

(C) Representative histograms of biexponentially transformed pSTAT1 flow cytometry signals in control and 15-min IFNγ-stimulated conditions, shown across the total sample (composite) and ontogeny classifications.

(D) Representative IC_{50} assay performed on patient blasts.

(E) Representative western blot analysis of AXL expression in patient blasts under control and IFNγ-exposed conditions for 24 h.

(F) Summary map of patient blasts integrating genetic profiles, percent blast ontogeny, z-scores of pSTAT1 SARA scores, IC_{50} baseline and fold change under IFNγ for quizartinib and gilteritinib, proliferation capacity fold change, and *Z* scores of AXL baseline expression and 24-h fold change post-IFNγ exposure.

(G–I) Correlation plots summarizing key relationships among quantified parameters. Outliers were removed using the interquartile range (IQR) method. Pearson correlation coefficients and *p*-values are indicated within the plot, and statistical significance was assessed using independent samples *t* test, where $p < 0.05$ (*), $p < 0.01$ (**), $p < 0.001$ (***), and n.s. = not significant. All quantified data points in this figure are summarized in Data S2.

phenotypic and functional properties. The inherent heterogeneity of patient samples presents a challenge in identifying fundamental cellular mechanisms. To address this, we tightly controlled experimental conditions and minimized variables to ensure a robust analysis. Given the complexity of AML, it is critical to measure multimodal parameters to accurately characterize blast behavior. In our experiments, we profiled the ontogeny of AML blasts while assessing key functional parameters, including pSTAT1 response to IFNγ, shifts in IC_{50} to FLT3 inhibitors, and AXL protein expression levels. Despite patient-to-patient variability, we identified trends supporting the IFNγ-STAT1 axis as a potential driver of resistance, mirroring our findings in cell line models. Specifically, we observed that certain blast samples exhibited drug resistance following IFNγ stimulation. Moreover, pSTAT1 response correlated with AXL expression, reinforcing the importance of STAT1 signaling in the regulation of resistance-associated pathways.

In conclusion, our study identifies IFNγ as a key driver of microenvironment-induced resistance in *FLT3*-mutated AML, mediated through STAT1-dependent AXL upregulation. These findings provide a mechanistic framework for understanding inflammatory signaling-driven resistance and offer potential therapeutic targets to enhance the efficacy of FLT3 inhibitors.

Limitations of the study

While this study provides mechanistic insights into IFNγ-driven resistance to FLT3 inhibitors in AML, several limitations should be acknowledged. First, the use of AML cell lines, while enabling controlled mechanistic dissection, inherently limits the scope of our findings due to their reduced microenvironmental complexity and clonal heterogeneity compared to primary patient samples. Second, although patient-derived blasts were incorporated to enhance translational relevance, these samples were cultured *ex vivo* under standardized conditions to achieve a uniform baseline prior to perturbation assays. This approach, while necessary for robust comparative analysis, introduces an artificial microenvironment that may not fully recapitulate the complex *in vivo* bone marrow niche, including stromal interactions, hypoxia, and cytokine gradients that influence drug response and resistance dynamics.

Third, while our data highlight the IFNγ-STAT1 axis as a dominant pathway mediating resistance, it is possible that IFNγ signaling indirectly activates additional survival pathways or other RTKs not captured in this study. The potential contribution of other RTKs, such as MER or TYRO3, as well as non-canonical IFNγ-induced signaling cascades, may play supporting roles in mediating resistance and warrant further investigation. Additionally, while our findings suggest that IFNγ acts in a paracrine-like manner within the microenvironment, the possibility of autocrine IFNγ signaling in AML blasts, particularly in highly inflamed niches, remains unexplored and could represent an additional layer of complexity in resistance mechanisms.

Lastly, while we employed genomic barcoding and longitudinal drug challenge assays to model resistance dynamics, these *in vitro* systems cannot fully capture the evolutionary pressures and cellular interactions present *in vivo*, including immune-mediated effects and pharmacokinetic factors influencing drug exposure. Despite these limitations, our integrative approach combining systematic perturbation, longitudinal tracking, and patient-derived sample validation provides a robust framework for dissecting microenvironmental contributions to drug resistance and identifies IFNγ-STAT1 signaling as a therapeutically relevant driver of resistance in FLT3-mutated AML.

RESOURCE AVAILABILITY

Lead contact

Further information and requests for resources and reagents should be directed to and will be fulfilled by the lead contact, P. Brent Ferrell (brent.ferrell@vumc.org).

Materials availability

For any reasonable requests regarding materials produced in this study, please contact the lead contact.

Data and code availability

- All data are available in the manuscript or the supplementary materials. The HDR donor plasmid map and FCS files from the study are hosted on Figshare (see key resources table). FASTQ files are hosted on SRA under the BioProject: PRJNA1215749.
- Script implementations and associated packages are available on GitHub (https://ferrell-lab.github.io/Khouqeer2025/) and archived on Zenodo (see key resources table).

ACKNOWLEDGMENTS

We thank Joseph Van Amburg for his assistance with NGS preparation, Amanda Hesterberg for her technical assistance with western blotting, and Tommy Chong for his thoughtful inputs. FACS sorting was performed at The VMC Flow Cytometry Core (P30 CA68485, DK058404) and the Veterans Affairs Flow Core. VANTAGE core services at Vanderbilt University performed the genomic sequencing. Computationally heavy analyses were conducted on the Advanced Computing Center for Research and Education (ACCRE) at Vanderbilt University. Funding: P.B.F. is supported by a Mark Foundation for Cancer Research Endeavor Award, a Novartis Global Scholar Award, NIDDK R56 (R56DK138826), VA MERIT award (I01BX005991). R.S.W. is supported by the Mark Foundation for Cancer Research Endeavor Award, NHLBI (R01HL150078 and 1PO1HL131477), and the O'Neal Comprehensive Cancer Center.

AUTHOR CONTRIBUTIONS

A.K.: conceptualization, methodology, software, validation, formal analysis, investigation, data curation, data analysis and interpretation, visualization, resources, supervision, writing – original draft, writing – review & editing. P.B.F.: conceptualization, methodology, data analysis and interpretation, writing – review & editing, supervision, project administration, and funding acquisition. J.C., C.K., K.M.D., C.R.P., A.E.G., and R.S.W.: technical and intellectual support.

DECLARATION OF INTERESTS

P.B.F. has received unrelated research funding from Novartis.

STAR★METHODS

Detailed methods are provided in the online version of this paper and include the following:

- KEY RESOURCES TABLE
- EXPERIMENTAL MODEL AND STUDY PARTICIPANT DETAILS
  - Cell lines
  - Human samples
- METHOD DETAILS

- IC_{50} assay and analysis
- Growth rate experiments and extrapolation
- Genomic barcoding and sequencing
- Lentivirus generation and transduction
- Drug challenge cycles and dynamics analysis
- RNAseq and analysis
- STAT1 genomic editing via CRISPR/Cas9 nickases
- Knockdown and inhibition of AXL and GAS6, and AXL overexpression
- Western blot and analysis
- AML patient blast functional analysis

- QUANTIFICATION AND STATISTICAL ANALYSIS

SUPPLEMENTAL INFORMATION

Supplemental information can be found online at https://doi.org/10.1016/j.isci.2025.114079.

Received: March 5, 2025
Revised: July 22, 2025
Accepted: November 13, 2025
Published: November 17, 2025

REFERENCES

1. Levis, M. (2013). FLT3 mutations in acute myeloid leukemia: what is the best approach in 2013? Hematology *2013*, 220–226. https://doi.org/10.1182/asheducation-2013.1.220.
2. Kottaridis, P.D., Gale, R.E., and Linch, D.C. (2003). Flt3 mutations and leukaemia. Br. J. Haematol. *122*, 523–538. https://doi.org/10.1046/j.1365-2141.2003.04500.x.
3. Nagel, G., Weber, D., Fromm, E., Erhardt, S., Lübbert, M., Fiedler, W., Kindler, T., Krauter, J., Brossart, P., Kündgen, A., et al. (2017). Epidemiological, genetic, and clinical characterization by age of newly diagnosed acute myeloid leukemia based on an academic population-based registry study (AMLSG BiO). Ann. Hematol. *96*, 1993–2003. https://doi.org/10.1007/s00277-017-3150-3.
4. Daver, N., Schlenk, R.F., Russell, N.H., and Levis, M.J. (2019). Targeting FLT3 mutations in AML: review of current knowledge and evidence. Leukemia *33*, 299–312. https://doi.org/10.1038/s41375-018-0357-9.
5. O'Donnell, M.R., Tallman, M.S., Abboud, C.N., Altman, J.K., Appelbaum, F.R., Arber, D.A., Bhatt, V., Bixby, D., Blum, W., Coutre, S.E., et al. (2017). Acute Myeloid Leukemia, Version 3.2017, NCCN Clinical Practice Guidelines in Oncology. J. Natl. Compr. Canc. Netw. *15*, 926–957. https://doi.org/10.6004/jnccn.2017.0116.
6. Larrosa-Garcia, M., and Baer, M.R. (2017). FLT3 inhibitors in acute myeloid leukemia: Current status and future directions. Mol. Cancer Ther. *16*, 991–1001. https://doi.org/10.1158/1535-7163.MCT-16-0876.
7. Zhao, J.C., Agarwal, S., Ahmad, H., Amin, K., Bewersdorf, J.P., and Zeidan, A.M. (2022). A Review of FLT3 Inhibitors in Acute Myeloid Leukemia. Blood Rev. *52*, 100905. https://doi.org/10.1016/j.blre.2021.100905.
8. Joshi, S.K., Nechiporuk, T., Bottomly, D., Piehowski, P.D., Reisz, J.A., Pittsenbarger, J., Kaempf, A., Gosline, S.J.C., Wang, Y.-T., Hansen, J.R., et al. (2021). The AML microenvironment catalyzes a stepwise evolution to gilteritinib resistance. Cancer Cell *39*, 999–1014.e8. https://doi.org/10.1016/j.ccell.2021.06.003.
9. Kennedy, V.E., and Smith, C.C. (2024). FLT3 targeting in the modern era: from clonal selection to combination therapies. Int. J. Hematol. *120*, 528–540. https://doi.org/10.1007/s12185-023-03681-0.
10. Wang, B., Reville, P.K., Yassouf, M.Y., Jelloul, F.Z., Ly, C., Desai, P.N., Wang, Z., Borges, P., Veletic, I., Dasdemir, E., et al. (2024). Comprehensive characterization of IFNγ signaling in acute myeloid leukemia reveals prognostic and therapeutic strategies. Nat. Commun. *15*, 1821. https://doi.org/10.1038/s41467-024-45916-6.
11. Naji, N.S., Sathish, M., and Karantanos, T. (2024). Inflammation and Related Signaling Pathways in Acute Myeloid Leukemia. Cancers *16*, 3974. https://doi.org/10.3390/cancers16233974.
12. Vadakekolathu, J., Minden, M.D., Hood, T., Church, S.E., Reeder, S., Altmann, H., Sullivan, A.H., Viboch, E.J., Patel, T., Ibrahimova, N., et al. (2020). Immune landscapes predict chemotherapy resistance and immunotherapy response in acute myeloid leukemia. Sci. Transl. Med. *12*, eaaz0463. https://doi.org/10.1126/scitranslmed.aaz0463.
13. Shaffer, S.M., Dunagin, M.C., Torborg, S.R., Torre, E.A., Emert, B., Krepler, C., Beqiri, M., Sproesser, K., Brafford, P.A., Xiao, M., et al. (2017). Rare cell variability and drug-induced reprogramming as a mode of cancer drug resistance. Nature *546*, 431–435. https://doi.org/10.1038/nature22794.
14. Gebru, M.T., Atkinson, J.M., Young, M.M., Zhang, L., Tang, Z., Liu, Z., Lu, P., Dower, C.M., Chen, L., Annageldiyev, C., et al. (2020). Glucocorticoids enhance the antileukemic activity of FLT3 inhibitors in FLT3-mutant acute myeloid leukemia. Blood *136*, 1067–1079. https://doi.org/10.1182/blood.2019003124.
15. Li, K., Du, Y., Cai, Y., Liu, W., Lv, Y., Huang, B., Zhang, L., Wang, Z., Liu, P., Sun, Q., et al. (2023). Single-cell analysis reveals the chemotherapy-induced cellular reprogramming and novel therapeutic targets in relapsed/refractory acute myeloid leukemia. Leukemia *37*, 308–325. https://doi.org/10.1038/s41375-022-01789-6.
16. Dumas, P.-Y., Naudin, C., Martin-Lannerée, S., Izac, B., Casetti, L., Mansier, O., Rousseau, B., Artus, A., Dufossée, M., Giese, A., et al. (2019). Hematopoietic niche drives FLT3-ITD acute myeloid leukemia resistance to quizartinib via STAT5-and hypoxia-dependent upregulation of AXL. Haematologica *104*, 2017–2027. https://doi.org/10.3324/haematol.2018.205385.
17. Wu, X., Liu, X., Koul, S., Lee, C.Y., Zhang, Z., and Halmos, B. (2014). AXL kinase as a novel target for cancer therapy. Oncotarget *5*, 9546–9563.
18. Ben-Batalla, I., Schultze, A., Wroblewski, M., Erdmann, R., Heuser, M., Waizenegger, J.S., Riecken, K., Binder, M., Schewe, D., Sawall, S., et al. (2013). Axl, a prognostic and therapeutic target in acute myeloid leukemia mediates paracrine crosstalk of leukemia cells with bone marrow stroma. Blood *122*, 2443–2452. https://doi.org/10.1182/blood-2013-03-491431.
19. Park, I.-K., Mundy-Bosse, B., Whitman, S.P., Zhang, X., Warner, S.L., Bearss, D.J., Blum, W., Marcucci, G., and Caligiuri, M.A. (2015). Receptor tyrosine kinase Axl is required for resistance of leukemic cells to FLT3-targeted therapy in acute myeloid leukemia. Leukemia *29*, 2382–2389. https://doi.org/10.1038/leu.2015.147.
20. Howard, G.R., Johnson, K.E., Rodriguez Ayala, A., Yankeelov, T.E., and Brock, A. (2018). A multi-state model of chemoresistance to characterize phenotypic dynamics in breast cancer. Sci. Rep. *8*, 12058. https://doi.org/10.1038/s41598-018-30467-w.
21. Viscarra, T., Buchegger, K., Jofre, I., Riquelme, I., Zanella, L., Abanto, M., Parker, A.C., Piccolo, S.R., Roa, J.C., Ili, C., and Brebi, P. (2019). Functional and transcriptomic characterization of carboplatin-resistant A2780 ovarian cancer cell lines. Biol. Res. *52*, 13. https://doi.org/10.1186/s40659-019-0220-0.
22. Sazonova, E.V., Yapryntseva, M.A., Pervushin, N.V., Tsvetcov, R.I., Zhivotovsky, B., and Kopeina, G.S. (2024). Cancer Drug Resistance: Targeting Proliferation or Programmed Cell Death. Cells *13*, 388. https://doi.org/10.3390/cells13050388.
23. McDermott, M., Eustace, A.J., Busschots, S., Breen, L., Crown, J., Clynes, M., O'Donovan, N., and Stordal, B. (2014). In vitro Development of Chemotherapy and Targeted Therapy Drug-Resistant Cancer Cell Lines: A Practical Guide with Case Studies. Front. Oncol. *4*, 40. https://doi.org/10.3389/fonc.2014.00040.
24. Bhang, H.e.C., Ruddy, D.A., Krishnamurthy Radhakrishna, V., Caushi, J.X., Zhao, R., Hims, M.M., Singh, A.P., Kao, I., Rakiec, D., Shaw, P., et al. (2015). Studying clonal dynamics in response to cancer therapy using high-complexity barcoding. Nat. Med. *21*, 440–448. https://doi.org/10.1038/nm.3841.

25. Chang, C.A., Jen, J., Jiang, S., Sayad, A., Mer, A.S., Brown, K.R., Nixon, A.M.L., Dhabaria, A., Tang, K.H., Venet, D., et al. (2022). Ontogeny and Vulnerabilities of Drug-Tolerant Persisters in HER2+ Breast Cancer. Cancer Discov. *12*, 1022–1045. https://doi.org/10.1158/2159-8290.CD-20-1265.

26. Siwek, W., Tehrani, S.S.H., Mata, J.F., and Jansen, L.E.T. (2020). Activation of Clustered IFNγ Target Genes Drives Cohesin-Controlled Transcriptional Memory. Mol. Cell *80*, 396–409.e6. https://doi.org/10.1016/j.molcel.2020.10.005.

27. van der Meer, J.H.M., van der Poll, T., and van 't Veer, C. (2014). TAM receptors, Gas6, and protein S: roles in inflammation and hemostasis. Blood *123*, 2460–2469. https://doi.org/10.1182/blood-2013-09-528752.

28. Gil, M.P., Bohn, E., O'Guin, A.K., Ramana, C.V., Levine, B., Stark, G.R., Virgin, H.W., and Schreiber, R.D. (2001). Biologic consequences of Stat1-independent IFN signaling. Proc. Natl. Acad. Sci. USA *98*, 6680–6685. https://doi.org/10.1073/pnas.111163898.

29. Kim, H.S., Kim, D.C., Kim, H.-M., Kwon, H.-J., Kwon, S.J., Kang, S.-J., Kim, S.C., and Choi, G.-E. (2015). STAT1 deficiency redirects IFN signalling toward suppression of TLR response through a feedback activation of STAT3. Sci. Rep. *5*, 13414. https://doi.org/10.1038/srep13414.

30. Eguchi, M., Minami, Y., Kuzume, A., and Chi, S. (2020). Mechanisms Underlying Resistance to FLT3 Inhibitors in Acute Myeloid Leukemia. Biomedicines *8*, 245. https://doi.org/10.3390/biomedicines8080245.

31. Vandewalle, N., De Beule, N., De Becker, A., De Bruyne, E., Menu, E., Vanderkerken, K., Breckpot, K., Devoogdt, N., and De Veirman, K. (2024). AXL as immune regulator and therapeutic target in Acute Myeloid Leukemia: from current progress to novel strategies. Exp. Hematol. Oncol. *13*, 99. https://doi.org/10.1186/s40164-024-00566-8.

32. Megger, D.A., Philipp, J., Le-Trilling, V.T.K., Sitek, B., and Trilling, M. (2017). Deciphering of the Human Interferon-Regulated Proteome by Mass Spectrometry-Based Quantitative Analysis Reveals Extent and Dynamics of Protein Induction and Repression. Front. Immunol. *8*, 1139. https://doi.org/10.3389/fimmu.2017.01139.

33. Zhou, T., Georgeon, S., Moser, R., Moore, D.J., Caflisch, A., and Hantschel, O. (2014). Specificity and mechanism-of-action of the JAK2 tyrosine kinase inhibitors ruxolitinib and SAR302503 (TG101348). Leukemia *28*, 404–407. https://doi.org/10.1038/leu.2013.205.

34. Holland, S.J., Pan, A., Franci, C., Hu, Y., Chang, B., Li, W., Duan, M., Torneros, A., Yu, J., Heckrodt, T.J., et al. (2010). R428, a Selective Small Molecule Inhibitor of Axl Kinase, Blocks Tumor Spread and Prolongs Survival in Models of Metastatic Breast Cancer. Cancer Res. *70*, 1544–1554. https://doi.org/10.1158/0008-5472.CAN-09-2997.

35. Yarden, Y., and Schlessinger, J. (1987). Self-phosphorylation of epidermal growth factor receptor: evidence for a model of intermolecular allosteric activation. Biochemistry *26*, 1434–1442. https://doi.org/10.1021/bi00379a034.

36. Hubbard, S.R., Mohammadi, M., and Schlessinger, J. (1998). Autoregulatory mechanisms in protein-tyrosine kinases. J. Biol. Chem. *273*, 11987–11990. https://doi.org/10.1074/jbc.273.20.11987.

37. Levine, J.H., Simonds, E.F., Bendall, S.C., Davis, K.L., Amir, E.a.D., Tadmor, M.D., Litvin, O., Fienberg, H.G., Jager, A., Zunder, E.R., et al. (2015). Data-Driven Phenotypic Dissection of AML Reveals Progenitor-like Cells that Correlate with Prognosis. Cell *162*, 184–197. https://doi.org/10.1016/j.cell.2015.05.047.

38. Goyal, Y., Busch, G.T., Pillai, M., Li, J., Boe, R.H., Grody, E.I., Chelvanambi, M., Dardani, I.P., Emert, B., Bodkin, N., et al. (2023). Diverse clonal fates emerge upon drug treatment of homogeneous cancer cells. Nature *620*, 651–659. https://doi.org/10.1038/s41586-023-06342-8.

39. Shaffer, S.M., Emert, B.L., Reyes Hueros, R.A., Cote, C., Harmange, G., Schaff, D.L., Sizemore, A.E., Gupte, R., Torre, E., Singh, A., et al. (2020). Memory Sequencing Reveals Heritable Single-Cell Gene Expression Programs Associated with Distinct Cellular Behaviors. Cell *182*, 947–959.e17. https://doi.org/10.1016/j.cell.2020.07.003.

40. Yoyen-Ermis, D., Tunali, G., Tavukcuoglu, E., Horzum, U., Ozkazanc, D., Sutlu, T., Buyukasik, Y., and Esendagli, G. (2019). Myeloid maturation potentiates STAT3-mediated atypical IFN-γ signaling and upregulation of PD-1 ligands in AML and MDS. Sci. Rep. *9*, 11697. https://doi.org/10.1038/s41598-019-48256-4.

41. Wang, A., and Zhong, H. (2018). Roles of the bone marrow niche in hematopoiesis, leukemogenesis, and chemotherapy resistance in acute myeloid leukemia. Hematology *23*, 729–739.

42. Dumas, P.-Y., Villacreces, A., Guitart, A.V., El-habhab, A., Massara, L., Mansier, O., Bidet, A., Martineau, D., Fernandez, S., Leguay, T., et al. (2021). Dual Inhibition of FLT3 and AXL by Gilteritinib Overcomes Hematopoietic Niche-Driven Resistance Mechanisms in FLT3-ITD Acute Myeloid Leukemia. Clin. Cancer Res. *27*, 6012–6025. https://doi.org/10.1158/1078-0432.CCR-20-3114.

43. Burchert, A., Attar, E.C., McCloskey, P., Fridell, Y.W., and Liu, E.T. (1998). Determinants for transformation induced by the Axl receptor tyrosine kinase. Oncogene *16*, 3177–3187. https://doi.org/10.1038/sj.onc.1201865.

44. Zhu, C., Wei, Y., and Wei, X. (2019). AXL receptor tyrosine kinase as a promising anti-cancer approach: functions, molecular mechanisms and clinical applications. Mol. Cancer *18*, 153. https://doi.org/10.1186/s12943-019-1090-3.

45. Spasic, M., Ogayo, E.R., Parsons, A.M., Mittendorf, E.A., van Galen, P., and McAllister, S.S. (2024). Spectral Flow Cytometry Methods and Pipelines for Comprehensive Immunoprofiling of Human Peripheral Blood and Bone Marrow. Cancer Res. Commun. *4*, 895–910. https://doi.org/10.1158/2767-9764.CRC-23-0357.

46. Ritz, C., Baty, F., Streibig, J.C., and Gerhard, D. (2015). Dose-Response Analysis Using R. PLoS One *10*, e0146021. https://doi.org/10.1371/journal.pone.0146021.

47. Smith, T., Heger, A., and Sudbery, I. (2017). UMI-tools: modeling sequencing errors in Unique Molecular Identifiers to improve quantification accuracy. Genome Res. *27*, 491–499. https://doi.org/10.1101/gr.209601.116.

48. Robinson, M.D., McCarthy, D.J., and Smyth, G.K. (2010). edgeR: a Bioconductor package for differential expression analysis of digital gene expression data. Bioinformatics *26*, 139–140. https://doi.org/10.1093/bioinformatics/btp616.

49. Schindelin, J., Arganda-Carreras, I., Frise, E., Kaynig, V., Longair, M., Pietzsch, T., Preibisch, S., Rueden, C., Saalfeld, S., Schmid, B., et al. (2012). Fiji: an open-source platform for biological-image analysis. Nat. Methods *9*, 676–682. https://doi.org/10.1038/nmeth.2019.

50. Romanski, A., and Bug, G. (2017). Establishment and Characterization of Long-Term Cultures Derived from Primary Acute Myeloid Leukemia Cells for HDAC Inhibitor Research. Methods Mol. Biol. *1510*, 127–148. https://doi.org/10.1007/978-1-4939-6527-4_10.

51. Weinreb, C., Rodriguez-Fraticelli, A., Camargo, F.D., and Klein, A.M. (2020). Lineage tracing on transcriptional landscapes links state to fate during differentiation. Science *367*, eaaw3381. https://doi.org/10.1126/science.aaw3381.

52. Sundararaman, B., Zhan, L., Blue, S.M., Stanton, R., Elkins, K., Olson, S., Wei, X., Van Nostrand, E.L., Pratt, G.A., Huelga, S.C., et al. (2016). Resources for the comprehensive discovery of functional RNA elements. Mol. Cell *61*, 903–913. https://doi.org/10.1016/j.molcel.2016.02.012.

53. Ewels, P.A., Peltzer, A., Fillinger, S., Patel, H., Alneberg, J., Wilm, A., Garcia, M.U., Di Tommaso, P., and Nahnsen, S. (2020). The nf-core framework for community-curated bioinformatics pipelines. Nat. Biotechnol. *38*, 276–278. https://doi.org/10.1038/s41587-020-0439-x.

54. Di Tommaso, P., Chatzou, M., Floden, E.W., Barja, P.P., Palumbo, E., and Notredame, C. (2017). Nextflow enables reproducible computational workflows. Nat. Biotechnol. *35*, 316–319. https://doi.org/10.1038/nbt.3820.

55. Layden, H.M., Eleuteri, N.A., Hiebert, S.W., and Stengel, K.R. (2021). A protocol for rapid degradation of endogenous transcription factors in mammalian cells and identification of direct regulatory targets. STAR Protoc. *2*, 100530. https://doi.org/10.1016/j.xpro.2021.100530.

56. Wiederschain, D., Wee, S., Chen, L., Loo, A., Yang, G., Huang, A., Chen, Y., Caponigro, G., Yao, Y.-M., Lengauer, C., et al. (2009). Single-vector inducible lentiviral RNAi system for oncology target validation. Cell Cycle *8*, 498–504. https://doi.org/10.4161/cc.8.3.7701.

57. Pedersen, C.B., Dam, S.H., Barnkob, M.B., Leipold, M.D., Purroy, N., Rassenti, L.Z., Kipps, T.J., Nguyen, J., Lederer, J.A., Gohil, S.H., et al. (2022). cyCombine allows for robust integration of single-cell cytometry datasets within and across technologies. Nat. Commun. *13*, 1698. https://doi.org/10.1038/s41467-022-29383-5.

STAR★METHODS

KEY RESOURCES TABLE

REAGENT or RESOURCE	SOURCE	IDENTIFIER
Antibodies		
Stat1 (D1K9Y)	Cell Signal	14994
Axl (C89E7)	Cell Signal	8661
GAS6 (D3A3G)	Cell Signal	67202
β-Actin (D6A8)	Cell Signal	8457
Anti-Rabbit IgG (H + L)	Promega	W4011
Anti-mouse IgG	Cell Signal	7076
HA-Tag (C29F4)	Cell Signal	3724
HLA-DR	BioLegend	307674
CD34	BD	569043
CD64	BioLegend	305010
CD123	BioLegend	306029
CD15	BioLegend	323033
CD33	BioLegend	303434
CD38	BioLegend	303506
CD45	BioLegend	304048
CD11b	BD	746704
CD117	BioLegend	313214
CD14	BioLegend	367143
Stat1 (pY701)	BD	612597
Biological samples		
AML patient blast samples	Vanderbilt University Medical Center Hematology Tissue Repository	Metadata in Data S2
Chemicals, peptides, and recombinant proteins		
Hyclone Fetal Bovine Serum	Cytiva	SH3091003HI
GlutaMAX	Gibco	35050061
Opti-MEM	ThermoFisher	31985062
cOmplete™, Mini, EDTA-free Protease Inhibitor Cocktail	Roche	11836170001
Alt-R™ HDR Enhancer V2	IDT	10007910
Cytarabine	selleckchem	S1648
Midostaurin	selleckchem	S8064
Quizartinib	selleckchem	S1526
Gilteritinib	selleckchem	S7754
Venetoclax	selleckchem	S8048
Bemcentinib	selleckchem	S2841
Ruxolitinib	selleckchem	S1378
AXL-Fc/soluble AXL (sAXL)	BioLegend	790902
Pacific Orange	ThermoFisher	P30253
hTPO	PeproTech	300–18
hSCF	PeproTech	300–07
hIL-3	PeproTech	200–03
IL-1RA	Peprotech	200-01RA
IL-10	MilliporeSigma	GF419

(*Continued on next page*)

Continued

REAGENT or RESOURCE	SOURCE	IDENTIFIER
IL-35	Peprotech	200–37
TGF-β	Peprotech	100–21
CCL23	Peprotech	300–29
FLT3L	Peprotech	300–19
GM-CSF	Peprotech	300–03
IL-3	Peprotech	200–03
VEGF	Peprotech	100–20
SCF	Peprotech	300–07
ANG-1	Peprotech	130–06
IFNα	Peprotech	592702
IFNγ	Peprotech	300–02
IL-17A	Peprotech	200–17
IL-1β	Peprotech	200-01B
IL-8	Peprotech	AF-200-08M
TNFα	Peprotech	300-01A
Critical commercial assays		
CellTiter-Glo® 2.0 Cell Viability Assay	Promega	G9241
DNeasy Blood & Tissue Kit	Qiagen	69504
RNeasy Mini Kit	Qiagen	74104
FuGENE® HD Transfection Reagent	Promega	E2311
Deposited data		
Healthy donor spectral flow datasets	Spasic et al.[45]	https://doi.org/10.6084/m9.figshare.25057739
Bulk RNAseq FASTQ files	This paper	Deposited to NIH SRA BioProject: PRJNA1215749
Barcode FASTQ files	This paper	Deposited to NIH SRA BioProject: PRJNA1215749
AML patient samples spectral flow datasets	This paper	https://doi.org/10.6084/m9.figshare.28281347
Experimental models: Cell lines		
MV411	ATCC	CRL-9591
MOLM13	AddexBio	C0003003
Oligonucleotides		
PCR primer sequences	This paper	Table S3
sgRNA sequences	This paper	Table S5
shRNA sequences	This paper	Table S6
Recombinant DNA		
pMD2.G	Addgene	12259
psPAX2	Addgene	12260
pUCIDT (Amp)	IDT	NA
Tet-pLKO-puro	Addgene	21915
pHAGE-AXL	Addgene	116714
HDR Donor plasmid	This paper	https://doi.org/10.6084/m9.figshare.28281347
Camargo Lab LARRY Barcode Library Version 1	Addgene	140024
Software and algorithms		
Drc	Ritz et al.[46]	https://doseresponse.github.io/drc/
umi_tools	Smith et al.[47]	https://github.com/CGATOxford/UMI-tools

(*Continued on next page*)

Continued

REAGENT or RESOURCE	SOURCE	IDENTIFIER
Nextflow	Di Tommaso et al.[26]	https://www.nextflow.io/
nf-core	Robinson et al.[25]	https://nf-co.re/
edgeR	Robinson et al.[48]	https://bioconductor.org/packages/edgeR
Fiji	Schindelin, J et al.[49]	https://github.com/fiji
cyCombine	Pedersen et al.[30]	https://github.com/biosurf/cyCombine
Phenograph	Levine et al.[37]	https://github.com/JinmiaoChenLab/Rphenograph
R (4.3.2)	Posit PBC	https://www.r-project.org
Python (3.9)	Python Software Foundation	www.python.org
SARAR	This paper	https://ferrell-lab.github.io/Khouqeer2025/; Archived at: https://doi.org/10.5281/zenodo.14741394).

EXPERIMENTAL MODEL AND STUDY PARTICIPANT DETAILS

Cell lines

MV411 (ATCC, CRL-9591) and MOLM13 (AddexBio, C0003003) AML cell lines were cultured in RPMI-1640 supplemented with 10% FBS and penicillin-streptomycin. HEK293T cells were cultured in DMEM supplemented with 10% FBS. Patient-derived AML blast cells were cultured as previously described, with a modification: TheraPEAK X-VIVO-10 Serum-Free Hematopoietic Cell Medium (Lonza, BP04-743Q) was supplemented with 10% Hyclone FBS (Cytiva, SH3091003HI), 1× (2 mM) GlutaMAX (Gibco), 25 ng/mL hTPO, 50 ng/mL hSCF, and 20 ng/mL hIL-3 (PeproTech).[50] All cells were maintained at 37 °C with 5% CO_2 in a humidified incubator.

Human samples

AML patient blast samples were obtained from the Vanderbilt University Medical Center Hematology Tissue Repository, with deidentified metadata in Data S2. All samples in the repository were enrolled via written informed consent for sample collection, and bone marrow aspirates were collected and processed by the Hematologic Tissue Repository at Vanderbilt University Medical Center (VUMC). Bone marrow mononuclear cells were cryopreserved and stored in liquid nitrogen until use. Deidentified data with limited demographic information was deposited in the repository metadata and used according to the protocol to access these samples approved by the local Institutional Review Board (#171654). All research on patient samples was conducted in accordance with the ethical standards of the institution and with the Declaration of Helsinki.

METHOD DETAILS

IC_{50} assay and analysis

As illustrated in Figure 1A, cell lines were seeded with designated microenvironment components (Table S1) or PBS control. Components were used at a final concentration of 10 ng/mL.

On day 1, cells were transferred to 96-well plates containing drug(s) (Table S2) and incubated for 48 h.

On day 3, 25 μL from each well was mixed with 25 μL of CellTiter-Glo 2.0 reagent (Promega, G9241), agitated for 5 min, and incubated for 5–10 min for signal stabilization before luminescence was measured using a GlowMax (Promega, Madison WI).

Luminance data were analyzed in R using the 'drc' package, with code available in the "IC_{50} Analysis" section of the accompanying GitHub repository.[46] Drug dose-response measurements were normalized to DMSO controls, and IC_{50} values were determined using a four-parameter log-logistic model. Statistical significance was assessed using a *t* test to compare IC_{50} ratios. Relative proliferation capacity was determined from the DMSO control viability measurements.

Growth rate experiments and extrapolation

Viability measurements from two time points were used to extrapolate growth rates. Growth rates were normalized to DMSO controls and analyzed in R. Detailed implementation code is available in the "Growth Rate" section of the accompanying GitHub repository.

Genomic barcoding and sequencing

The LARRY Barcode Version 1 library (Addgene, 140024) was expanded, packaged into lentivirus, and transduced into cell lines as previously described.[51] Briefly, the library was first expanded in DH10B cells cultured in sixty 10 cm Petri dishes. Plasmids were then purified using a standard Maxi prep kit. The purified library was subsequently used to generate lentivirus, as detailed in the lentivirus generation and transduction section. Library diversity was confirmed by Next-Generation Sequencing (NGS) (Figure S2B).

To sequence barcodes, DNA was extracted using the DNeasy kit (Qiagen, 69504). The barcode region was amplified using LARRY primers, followed by a second PCR to add Illumina adapters (see Table S3 for primer sequences). and the samples were sequenced on an Illumina Nova X Plus (Illumina, San Diego, CA).

FASTQ files were processed using Python and the umi_tools package.[47] Detailed implementation code is available in the "Barcode Analysis" section of the accompanying GitHub repository, and FASTQ files have been deposited in Sequence Read Archive (SRA) (see resource availability).

Lentivirus generation and transduction

Lentiviral vectors were developed using pMD2.G and psPAX2, as previously described (Addgene, 12259, 12260).[52] Briefly, pMD2.G, psPAX2, the lenti plasmids, and FuGENE HD transfection reagent (Promega, E2311) were combined in Opti-MEM (ThermoFisher, 31985062) at specified ratios (Table S4). After incubating for 20 min, the mixture was added dropwise to 10 cm dishes containing HEK293T cells at 50% confluency. The supernatant was collected over three days, pooled, and ultracentrifuged at 100,000 × g for 90 min. AML cell lines were transduced via spinfection (1200g for 90 min) using the concentrated lentivirus. Cells were expanded and GFP-sorted 5–7 days post-transduction.

Drug challenge cycles and dynamics analysis

Cells were seeded in 12-well plates at 0.5–1 million cells/mL in 2 mL of media and maintained at this density throughout the assay. For each challenge cycle, cells were treated with drug at the respective IC_{50} concentrations (quizartinib: 3.77 nM; gilteritinib: 31.02 nM) and incubated for either 5 h or 16 h. The initial 5-h incubation period was determined empirically based on its ability to induce measurable cell death while maintaining viability. Once cells in the control condition exhibited resistance, indicated by recovery of growth rate to baseline levels, the incubation period was extended to 16 h to continue monitoring resistance dynamics. After drug incubation, the media was replaced, and a baseline viability measurement was recorded. A second viability measurement was taken 24 h later to assess growth recovery using CellTiter-Glo 2.0.

RNAseq and analysis

RNA was extracted using the RNeasy Mini Kit (Qiagen, 74104), and sequencing was performed at Mirxes. FASTQ files have been deposited in SRA (see resource availability). FASTQ files were processed and mapped using Nextflow and the nf-core/RNAseq default workflow.[53,54] Differential expression and Gene Ontology (GO) analysis was performed in R using the edgeR package.[48]

STAT1 genomic editing via CRISPR/Cas9 nickases

A PAM-out nickase approach was used to introduce single-stranded cuts near the stop codon of the STAT1 gene. A cloning plasmid (IDT, pUCIDT-AMP) was modified to serve as the homology-directed repair (HDR) donor by incorporating the STAT1 sequence from the cut site to the stop codon, $FKBP12^{F36V}$ degron tag, HA-tag, P2A, and mCherry sequences. These elements were flanked by a 5′ homology arm (200 bp) and a 3′ homology arm (450 bp). The HDR donor plasmid map is available on the accompanying Figshare.

Electroporation components and protocols were followed as previously described.[55] A summary of the components is provided in Table S5. Briefly, a ribonucleoprotein (RNP) complex was assembled in a modified R buffer (250 mM sucrose, 1 mM $MgCl_2$ in PBS). MV411 cells were resuspend in 105 μL of R buffer. To the cell suspension, 12 μg of HDR plasmid concentrated in 2 μL and 1.9 μL of 100 μM Alt-R HDR Enhance r V2 (IDT, 10007910) were added. The cells were then mixed with the RNP complex.

Electroporation was carried out using the NEON Electroporation System (ThermoFisher) with 100 μL tips and the following settings: 1 pulse at 1,350 V for 35 ms. After electroporation, cells were plated in a 6-well dish containing antibiotic-free media and expanded for one week. Enrichment for mCherry-positive cells was performed twice by FACS (Figure S3B). Cassette insertion was validated via HA-tag Western blot (Figure S3C). Phosphorylation of the modified STAT1 protein was validated by stimulating cells with IFNγ for 15 min, followed by intracellular flow cytometry to measure phosphorylated STAT1 levels (Figure S3D). To isolate a homozygous edited clone, single-cell sorting was performed, and the resulting clones were screened using a 3-primer melt curve analysis system (Figures S3E–S3G).

Knockdown and inhibition of AXL and GAS6, and AXL overexpression

Knockdowns were performed using the Tet-pLKO-puro plasmid (Addgene, 21915). AXL and GAS6 shRNA sequences (Table S6) were cloned into the plasmid using the standardized pLKO plasmid cloning protocol.[56] An shRNA scramble control with the same shRNA system was performed (Addgene, 192076) (Figure S3H). Modified plasmids were used to generate lentiviral particles for cell transduction. Three days post-transduction, puromycin selection (0.5 μg/mL) was maintained for 5 days. Knockdown was induced with 2 μg/mL doxycycline. Knockdown efficiency was confirmed via Western blot.

AXL activity was inhibited using Bemcentinib (Selleckchem, S2841). A dose-response experiment (Figure S3I) determined 61.8 nM as the highest non-toxic dose. Soluble AXL (sAXL) (BioLegend, 790902) was added at the specified concentrations.

Overexpression of AXL was achieved by packaging and transducing the pHAGE-AXL plasmid (Addgene, 116714).

Western blot and analysis

Cells were lysed in RIPA buffer supplemented with a protease inhibitor cocktail (Roche, 11836170001). The lysates were boiled in Laemmli buffer containing dithiothreitol (DTT) for 10 min and loaded onto a 4–20% polyacrylamide gel (Bio-Rad, 4561094). Electrophoresis was performed in Tris-Glycine-SDS buffer.

Protein transfer was carried out using the Trans-Blot Turbo Transfer System (Bio-Rad) onto PVDF membranes. The membranes were blocked in 5% milk TBST for 24 h at 4°C with gentle rocking. Antibody details, including dilutions and incubation times, are summarized in Table S7. Membranes were developed using Pierce ECL substrate (ThermoFisher, 32106). Protein band quantification was performed using Fiji.[49]

AML patient blast functional analysis

AML patient blast samples were obtained from the Vanderbilt University Medical Center Hematology Tissue Repository, with repository numbers listed in Data S2. Samples were thawed, counted, and split among conditions as below.

One portion was split into two conditions: 1) PBS control and 2) IFNγ-stimulated for 15 min. After stimulation, cells were fixed in 1.6% PFA and permeabilized in ice-cold methanol. Barcoding was performed using Pacific Orange (PO) (ThermoFisher, P30253) at two distinct concentrations (high: 100 ng/mL, low: 12 ng/mL). The barcoded cells were washed, pooled, and stained with an antibody cocktail (Table S7). Spectral flow cytometry was conducted using the Cytek Aurora (Cytek Biosciences, CA). FCS files are available on the accompanying Figshare.

FCS files were processed in R by gating blast cells based on forward and side scatter (Figure S5A) and subsetting them according to PO barcoding (Figure S5B). Healthy donor spectral flow datasets from Spasic et al. were normalized with AML FCS files using cyCombine.[45,57] (Figures S6A and S6B) The healthy donor normalized datasets were embedded in UMAP space to generate a reference embedding. Phenograph clustering was subsequently applied to identify relevant clusters.[37]

The AML cells were projected into the UMAP space, and their UMAP coordinates were compared to the centroids of reference clusters (progenitors, monocytes, and dendritic clusters) using cosine similarity. Detailed implementation code for this analysis is available under the ''Ontogeny'' section in the accompanying Github repository.

To evaluate the perturbation of STAT1 phosphorylation in response to IFNγ, we developed SARAR, an R-based implementation of SARA (Statistical Analysis of Perturbation Response).[37] The detailed implementation code and a deployable R package are available under the ''SARAR'' section in the accompanying Github repository. A SARA score was generated for each blast by comparing control and stimulated conditions, and the scores were scaled to z-scores for interpretability.

The second portion of cells was used for IC_{50} determination of quizartinib and gilteritinib under control and IFNγ conditions. Additionally, AXL expression was evaluated via Western blot

QUANTIFICATION AND STATISTICAL ANALYSIS

Drug dose-response measurements were normalized to DMSO controls, and IC_{50} values were determined using a four-parameter log-logistic model. Statistical significance was assessed using a *t* test to compare IC_{50} ratios. Relative proliferation capacity was determined from the DMSO control viability measurements. Statistical significance was determined based on the estimated *p*-values of the designated statistical test in each figure panel, where $p < 0.05$ (*), $p < 0.01$ (**), $p < 0.001$ (***), and n.s. = not significant. Statistical details are stated in each figure and figure legend.